Coarsening of grain refined semi-solid Al-Ge32 alloy: X-ray microtomography and in situ radiography

S. Zabler*, A. Rueda and A. Rack+

Hahn-Meitner-Institute Berlin, Structural Research SF-3, Glienicker Str. 100, 14109 Berlin, Germany
* corresponding author: Email simon.zabler@hmi.de, phone +49 (0)30 8062 2822, FAX +49 (0)30 8062 3059
+ current address: Forschungszentrum Karlsruhe ANKA, 76344 Eggenstein-Leopoldshafen, Germany

H. Riesemeier

Federal Institute of Materials Research and Testing (BAM), Unter den Eichen 87, 12205 Berlin, Germany

P. Zaslansky

Max Planck Institute of Colloids and Interfaces, Wissenschaftspark Golm,14424 Potsdam, Germany

I. Manke, J. Banhart

TU Berlin (PN2-3), Hardenbergstraße 36, 10623 Berlin, Germany

Abstract

The Lifshitz, Slyozov and Wagner theory (LSW) describes the coarsening of low volume fraction dispersed particles in a supersaturated solution as governed by a $t^{1/3}$ power law, while stating that ripening occurs in a self-similar manner. Only few experiments report the 3D coarsening in binary semi-solid alloys which differs from the LSW theory. We report here on in-situ Al-Ge32(wt.%) coarsening, used as a model system for a large variety of technical alloys. Numerical analysis of 2D and 3D images of the microstructure measured by X-ray radiography and microtomography reveals the evolution of the solid particles during annealing. Ripening of a grain-refined particles network is found to be quite well described by LSW theory although somewhat smaller exponents ($t^{1/4}$~$t^{1/5}$) are found. Changes in the coarsening behavior are observed in samples which are thinner than 0.5*mm* as well as for non equiaxed alloy microstructures, characterized by anisotropic dendrites.

Keywords: Microtomography, Radiography, 2D/3D image analysis, technical binary alloys, LSW

1. Introduction

The microstructure of binary metallic alloys such as Al-Si and Al-Ge is characterized by a primary solid phase and an eutectic phase: during solidification the primary solid phase nucleates at the liquidus temperature and continues to grow until the solidus temperature is reached and the remaining melt freezes, forming the fine structured eutectic phase. The resulting primary solid phase microstructure depends to a large extent on the cooling rate and the distribution of nucleation sites, and it is desirable that a globular microstructure forms. Whenever pre-alloyed metals are partially remolten and are then annealed at a temperature above the solidus, as often occurs in industrial casting processes, coarsening of the primary solid is observed.[1,2] The coarsening occurs due to dissolution of the eutectic phase, which results in additional 'ripening' of the solid phase.[3,4] In particular, during rheo- and thixocasting, the alloy is heated to the semi-solid state before it is cast[5,6] (for reliable and successful casting processes and obtaining the designed final components, stringent control over the microstructure is crucial). The morphology of the primary phase can coarsen in various ways when an alloy is held in the semi-solid state during processing.[7] Many parameters contribute to this variation, including flow of the slurry, temperature and possibly sample dimensions.[8,9] Under the assumption that the primary phase forms an agglomeration of many particles, coarsening is considered to be the result of two processes: isolated particles grow at the expense of smaller particles[10,11] (cf. Fig 1a) or connected "touching" particles merge into larger particles by coalescence[12,13] (Fig. 1b). These descriptions are of course only models, because in reality many technical-alloys form semi-solid skeletons that coarsen in a different way (see Fig. 1c).

The partition of solid (S) and liquid (L) phases in binary alloys can be expressed in terms of volume fractions g_S and g_L (note that $g_S + g_L = 1$). During annealing, the solid particles change their volume and grow. The average volume, which for sufficiently round particles

can be approximated to be proportional to the cube of the average diameter, increases linearly with the annealing time, according to

$$d(t)=K\left(t-t_0\right)^{1/3} \quad (1)$$

Here, *d(t)* is the average diameter at time *t*, t_0 the time when d=0 and *K* is the growth rate and the coarsening exponent is 1/3 according to Lifshitz, Slyozov and Wagner (LSW-theory).[14,15] Equation 1 is considered a valid description for growth and coarsening of spherical particles in a supersaturated solution. The LSW theory also claims that at any time during coarsening, the average particle diameter maintains a constant ratio to the width of the particle diameter distribution at any given time. Consequently, self-similarity is an expected characteristic of the structure as it coarsens.

One of the assumptions of the LSW theory is that g_s has to be small, so that individual particles may be considered 'non interacting'. A small g_s is fundamental to the interpretation of many of the dynamic processes that are related to coarsening. This is because moderate g_s values result in interactions between neighboring grains, that bring about higher concentration gradients in the liquid while increasing *K*.[16-18] For semi-solids we note that with g_S exceeding a percolation threshold (all particles become interconnected) the particles start to form a three-dimensional skeleton which is characterized by agglomerates that make identification of single particles difficult.[17,19]

The *liquid film migration* model[20] extends LSW further to include significantly higher solid fractions than originally proposed, accounting for connected particles whereby mass transfer occurs along the connection necks. Most experimental models explicitly predict broader size distributions of particles, compared to the ideal dispersion that was considered in the LSW theory. Theoretical predictions of the dynamics of the process have provided possible explanatory mechanisms for deviations from classical LSW theory.[21] Despite these differences, coarsening theories confirm Eq. 1 and most assumptions result in similar linear

relationships between average particle volume and annealing time. By using scaling functions and assuming self-similar statistical ensembles, the universality of the $t^{1/3}$ growth has been demonstrated in three-dimensions for a variety of phase-separating processes.[22] Recently it has been shown that even for anisotropic metallic microstructures consisting of dendrites, the $t^{1/3}$ relation holds, if *d(t)* in Eq. 1 is replaced by a length scale characteristic of the solid-liquid interface.[23] Exponents of 1/4 and 1/5 are thought to be related to the coarsening of precipitates located at grain boundaries and dislocations respectively. However, even these cases are only different from LSW if volume diffusion is truly negligible.[21]

To the best of our knowledge, only few in situ measurements have provided direct evidence for any of the theoretical predictions of coarsening of a semi-solid network of binary metallic alloys.[24] What is known about the evolution of the particle size distribution is mainly based on measurements obtained from 2D images[2,25,26] and much remains unknown about the 3D coarsening. Current state-of-the-art technology allows to visualize the 3D characteristics of the particles of the primary solid, allowing to provide direct answers to many questions. In this work, the coarsening of a non-agitated semi-solid network of particles (cf. Fig. 1c) is monitored in grain refined Al-Ge32(wt.%) alloy. When this alloy is heated to a temperature above the solidus and below the liquidus, a dispersion of solid Al-rich particles in a liquid Al-Ge solution takes place. In contrast to the destructive and time-consuming serial sectioning methods[17,19,23,27] we use non-destructive x-ray imaging to produce dynamic radiographs and static tomograms of the microstructure in a binary aluminum-germanium alloy of Al-Ge32. These data are then used to quantify various coarsening parameters such as the particle size, nearest-neighbor characteristics and connectivity.

2. Materials

2.1 Grain refined Al-Ge32 alloy

The binary alloy Al-Ge32 was selected for this investigation because its structural properties are most similar to the important class of casting alloys based on Al-Si7 (e.g. A356). To create a microstructure comparable to Al-Si7 a composition of 68 wt.% Al and 32 wt.% Ge was chosen to yield a 0.5 volume fraction of the α-particles at the eutectic temperature T = 420º C. Aluminum and silicon have very similar x-ray absorption coefficients, which is why the Al-Si7 alloy microstructure cannot be resolved by standard x-ray imaging techniques. The higher atomic mass of germanium generates strong absorption contrast relative to aluminum when x-ray images are observed, making it much more amenable to this type of investigation. The simple-eutectic equilibrium binary phase-diagram[28] of Al-Ge is depicted in Fig. 2. A homogeneous equiaxed distribution of fine aluminum α-grains embedded in a matrix of the eutectic composition was produced by melting and quenching Al-Ge32 ingots. The ingots were formed by combining the pure elements (>99.99%) with 4 wt.% commercial Al-Ti5-B grain refiner (KBM AFFILIPS, Netherlands) followed by levitation melting and casting in a cold crucible. The grain refiner was used to reduce the grain size and to minimize directional growth of dendrites during solidification.[29,30] This occurs due to the sub-micrometer sized titanium boride particles that increase the number of nucleation sites for α-Al. Fig. 2 illustrates the difference between grain refined produced microstructure (a) and dendritic non grain refined microstructure (b) of Al-Ge32 alloy.

2.2 Sample preparation and annealing

Samples for radiography and tomography were cut from the cast Al-Ge32 ingot. For the radiography experiments thin foils of Al-Ge32 were used for the purpose of observing the ripening of solid Al-particles in the melt in situ. Foils of thicknesses: 0.1 *mm*, 0.2 *mm*, 0.4 *mm* and 0.5 *mm* each 3 *mm* x 3 *mm* in width and height were used. During radiography the samples were annealed at a constant temperature of 450º C (470º C for the 0.5 *mm* foil to improve the visibility of the solid particles by reducing the solid volume fraction).

Heat absorption was measured during remelting of the Al-Ge32 alloy using a differential scanning calorimeter and the weight fractions f_S = 0.41 at 450º C and f_S = 0.37 at 470º C were found by integration of the heat flow graph. Taking the concentrations $C^{(S)}$ *and* $C^{(L)}$ of solid and liquid from the phase diagram in Fig. 2 and the densities $\rho_{Al}^{(L)} = 2.4 g/cm^3$, $\rho_{Ge}^{(L)} = 5.6 g/cm^3$, $\rho_{Al}^{(S)} = 2.6 g/cm^3$ and $\rho_{Ge}^{(S)} = 5.3 g/cm^3$ of solid (S) and liquid (L) aluminum and germanium, we calculated the volume fractions g_S = 0.49 at 450°C and g_S = 0.45 at 470°C using the method of partial areas:

$$g_S = \frac{f_S}{f_S + (1 - f_S)\dfrac{\rho_S(C,T)}{\rho_L(C,T)}} \tag{1}$$

For the tomography experiment, a cylindrical sample 6 *mm* in diameter and approx. 15 *mm* high was cut out of the ingot that provided the samples for radiography. The sample was repeatedly heat-treated by annealing at T=450º C for 8 minutes followed by air cooling. Prior to and following each treatment, complete tomograms were recorded. Altogether 6 3D images of the cylindrical sample were obtained, with the last tomogram, corresponding to a total cumulated annealing time of 40 minutes. A second cylinder of a non grain refined alloy of the same dimensions was heat-treated and imaged similarly. This sample, which contained an initial dendritic microstructure (cf. Fig. 3b), was used for comparison.

3. Image acquisition

Radiography and tomography were carried out at the Berlin synchrotron BESSY on the BAM*line*.[31] Fig. 4 illustrates the experimental setup for radiography as well as a typical image obtained during such experiments.

The Al-Ge32 foils were clamped between two 1 *mm* thick boron nitride (BN) plates which are almost completely transparent for x-rays, allowing placement in the beam. Temperature was monitored by a thermocouple element placed close to the alloy. The photon energy for

the radiography experiments was set to E = 25 *keV*. We inserted each Al-Ge foil into the BN sample holder in which the experiment took place. The temperature, number of images (at 0.23 fps) and effective annealing time (during which the material was in the semi-solid state) are listed in table 1. Images were acquired using a thin x-ray converter screen of YAG:Ce single crystal (Saint Gobain SA, France) coupled to a CCD camera and magnification lenses, commonly used in synchrotron x-ray imaging. The effective pixel size was $\Delta x = 1.6\ \mu m$ and the optical resolution was 6-7 μm.[32] As can be seen from Fig. 4a the necessity to maintain the sample in the focus of two heating lamps prevented us from moving the sample out off the beam in order to record brightfield images (best suited for normalization). To correct for beam inhomogeneities (seen as blurred horizontal lines overlying the silhouette of the sample, shown in Fig 4b) a virtual brightfield image was created by applying a stripe-shaped median-filter and assuming slow horizontal modulations in the intensity. The experimental radiographs were then normalized by this corrective background (schematically illustrated in Fig. 5) by simple division, as is usually done in tomographic imaging. An example of the resulting images at annealing times of 3 min and 33 min is shown in Fig. 6, along with a metallurgical micrograph of a polished section of the same sample, shown for comparison.

Tomography provided quantitative results about the three-dimensional particle network and the true particle sizes. Tomographic imaging at synchrotron facilities, as was used in these experiments has been reported elsewhere.[33-35] A scintillator screen of quartz glass coated with 10 μm gadolinium oxisulfide (GADOX) powder was used for the data acquisition reported here, with the resulting pixel size of $\Delta x = 3.5\ \mu m$ and an optical resolution limited by the thickness of the GADOX layer to approx. 12 μm. For each tomographic recording we acquired 900 angular projections using x-rays of E = 50 *keV* photon energy. The six measurements were aligned so as to allow matching the particles allowing comparison of the differences in microstructure.

4. Data analysis

Numerical image analysis was used to identify and quantify the primary solid phase. Both radiography and tomography produced data where different grey values, assigned to each pixel (voxel in 3D), represented the extent of x-ray absorption at each point. A histogram calculated for a typical image is shown for example in Fig. 7a. For a two phase system such data can be further simplified by threshold binarization, i.e. setting every value above a threshold to '1' (foreground, values to the right of the dashed line in Fig. 7a, correspond to primary solid phase), and all other values to '0' (background). All 2D radiographs and 3D tomograms were binarized in this way, and a method of segmentation was then used to identify and separate particles: each group of foreground pixels was labeled and measured, determining such attributes as particle size and connectivity, along the following guidelines:

Initially, a 3 × 3 mean filter was applied for smoothing (3 × 3 × 3 for 3D data), to suppress the high frequency noise (Fig. 7b). The time-series radiographs were further normalized by setting the mean gray value to zero and the standard deviation of the distribution to one. The 2D/3D images were then binarized as shown in Fig. 7c and used to calculate Euclidean distance transform maps[36] (EDT, see Fig. 7d). In such EDT maps, every point corresponding to foreground pixels contains a value representing the distance (in pixels) to the nearest background point, and similar - but inverse - values are calculated for points corresponding to background pixels.[37] The maxima in these maps represent the centers of the particles, and the minima represent points at equal distance between neighboring particles. These maps were used to identify the boundaries of each particle using 'region growing' also known as 'Watershed transformation' (Fig. 7e)[38,39] which, following multiplication by the binary image (Fig 7c) allowed automatic identification of each particle, its position and size (Fig. 7f). While calculations in 3D were done with MAVI,[40] we used ImageJ[41] for binarization and watershedding of 2D images. We note that in order to prevent over-segmentation in 3D with this procedure, whereby non-spherical particles become artificially fragmented, a pre-flooding

algorithm was used to exclude very small particles and speckles from the analysis.[42] In this manner particles smaller than 12 μm were merged with their larger neighbors. The labeled and segmented 3D data allowed to calculate connectivity n (average number of contacts per particle) and contiguity of the particles: contiguity G^S describes the fraction of a particle's surface that is connected to neighboring particles,[40] commonly defined by average values:

$$G^S = \frac{2S^{SS}}{2S^{SS} + S^{SL}} \quad (2)$$

with S^{SS} the average solid-solid interface, equivalent to the fraction of surface area of a particle that is connected to neighboring particles (accounted for twice in eq. 2 due to the existence of a single connection between two adjacent particles) and S^{SL} the average remaining particle-matrix interface. $G^S = 0$ for isolated particles and $G^S = 1$ for solid phase only.

The average particle diameter and standard deviations were calculated from the 2D/3D images and the data was fit to a power law similar to eq. 1 (Origin7.0, Northhampton, MA, USA). Due to the fact that the choice of the binarization threshold has an effect on these results, we tested a wide range of thresholds for each sample.

5. Results

5.1 In situ radiography

Fig. 8 is a plot of the coarsening exponent calculated for several binarization thresholds which correspond to solid area fractions between 20% and 80%. The calculated exponents show minimal scatter and we note that their value is almost constant for solid fractions between 40% and 60%. We therefore chose a binarization threshold of approx. 50% for the analysis of all the datasets.

Results for the average particle diameters $<d>$ and the standard deviation (SD) in 2D as a function of annealing time are given in Fig. 9 for the four different sample thicknesses (solid

lines represent the fit). As can be seen, following an initial plateau prior to reaching the annealing temperature, a significant rise in average particle diameter is observed. With increasing annealing time the coarsening slows down. The standard deviation of average particle diameter is shown as an inset in each graph, attesting to the fact that the width of the diameter distribution increases concomitant with the average values. The sample thickness, annealing temperature, calculated growth rates and exponents are shown along with their corresponding error values in table 1. We note that a median filter of size 7 x 7 was applied to the images recorded from the thinnest sample. This was done because the 0.1 *mm* of Al-Ge32 created only weak contrast, resulting in poor signal to noise ratios due to the strong signal from the BN sample holder and the beam.

5.2 X-ray microtomography

Distributions of particle diameter, contiguity and connectivity of the six 3D datasets of the grain refined alloy and four datasets of the non grain refined alloy recorded at different annealing times are shown in Fig. 10. Particle diameters (panels a and b) and particle contiguity (panels c and d) were fitted with Gaussian distributions while connectivity was fitted to a log-normal distribution function (panels e and f). As can be seen, the average particle diameter as well as the width of each distribution increase during annealing, shifting from ~70 to 100 microns in the grain refined and from 75 to 110 microns in the non grain refined sample. Contiguity of the grain refined alloy shows only minor changes in the average values (approx 0.21) while for the non grain refined alloy contiguity only starts around 0.1 and increases with the annealing time. No significant shift of the maximum connectivity in the grain refined sample (approx. 4) is observed. For the non grain refined alloy connectivity drops from about 5 to 4. All distributions show the total number of particles to decrease with increasing annealing time. For the 3D data, <d>, (SD) and the ratio <d>/(SD) of the diameter distributions as well as maximum connectivity and contiguity G^S are shown in table 2.

The coarsening of a small particle cluster is shown in Fig. 11. In this figure, grain refined and non grain refined alloy microstructures are shown together with the results obtained from fitting <d> to a power law similar to Eq. 1 (dashed lines show the confidence intervals of the fit). For the grain refined alloy we obtain a rate K=41.5 +/- 2.5 with a growth exponent 0.21 +/- 0.02, and for the non grain refined alloy K=32 +/- 12 and the exponent 0.30 +/- 0.08.

6. Discussion

This work reports on experimental results of dynamic and quasi-dynamic coarsening of semi-solid Al-Ge microstructure which was used as a binary model system for common Al-based engineering alloys. By direct comparison between 2D real-time radiographs and frozen intermediate 3D tomographic datasets we show the dynamics of microstructural evolution in the semi-solid state. We find a significant difference between grain-refined and non grain-refined alloys: while the grain-refined alloy is shown to fulfill the criteria for self-similar coarsening predicted by the LSW theory, the same alloy but without additional grain-refiner does not. By comparison of the bulk Al-Ge32 microstructure with observations from thin foils we find significant deviations in the coarsening dynamics when the sample thickness decreases, approaching the average particle size. Detailed 2D/3D analysis was used for image segmentation, labeling and quantification of the primary Al-particles. To the best of our knowledge this is the first time that such a method has been applied to the study of dynamics of 3D alloy coarsening of agglomerated non-spherical particles.

Both from observations of thin foils and bulk samples we find the microstructure of semi-solid Al-Ge32 alloy to evolve in reasonably good agreement with the $t^{1/3}$ power law which is predicted by classical LSW theory.[14,15] Thus coarsening of a solid network of agglomerated particles in a liquid solution is well described by considering the particles as separate entities. By measuring their size distribution as a function of annealing time we have found that the evolution of a network consisting of round but non-spherical particles is very similar to the

coarsening of dispersed spherical particles which is described by the LSW theory. The transition from bulk samples to thin foils of thicknesses which approach the average particle diameter does not appear to significantly alter the coarsening law.

The self-similar character of the coarsening in a network is an important statement of LSW theory: For dispersed spherical particles, the ratio of the average diameter versus the width of the diameter distribution is time-independent. Our findings show this to be true for a network of agglomerated Al-particles in the Al-Ge32 system that we used in our experiments. Additionally we found that two parameters which characterize self-similar growth of a particle network, namely the distributions of particle connectivity and contiguity, maintain constant maximum values, independently of the annealing time. We conclude that at any given time at which we observe a particle in a coarsening semi-solid network, the number of connections to other particles, the relative size of the connecting necks and the normalized size distribution of the surrounding particles appear to be constant. The maximum connectivity of the equiaxed Al-particles was found to be ~3.6 which is in excellent agreement with recent studies reported on Sn-Pb alloy where a value of 3.66 was found for g_s=0.52.[36] Rowenhorst et al. showed for this system that the average connectivity is mainly a function of g_s, reaching values of 8~9 for g_s>0.7. Similar to their work on Sn-Pb, our data also reveals a correlation between particle diameter and connectivity where larger particles exhibit a higher number of contacts.

For comparison we produced a non-equiaxed microstructure simply by leaving out the additional grain-refiner. In contrast to the segmentation of equiaxed grain-refined Al-Ge32 microstructure, numerically segmenting elongated Al-dendrites which characterize the non-equiaxed structure results in virtual particles that are strongly asymmetric. Using a different approach based on parameterization and curvature analysis of the solid-liquid interface, Mendoza et al. 2004 have recently shown violation of the self similarity in the coarsening of

non-equiaxed Al-Cu alloy.[23] Applying the criteria for self-similar growth of particle networks to our data, we find a similar violation for the Al-Ge32 system. In particular, we observe connectivity to decrease and contiguity to increase during the annealing of the non equiaxed structure which is in contradiction to self-similar growth. Compared to grain-refined Al-Ge32 structure at similar annealing times, average particle size and contiguity are larger while contiguity is smaller: This can be interpreted as a direct result of the elongated asymmetric shape of the dendrites which is maintained during the coarsening. Extending their approach Mendoza et al. have also shown that the non-equiaxed Al-Cu microstructure evolves towards an anisotropic morphology aligned with the orientation of solidification.[43] In Al-Ge32 alloy we find slightly different coarsening rate and exponent for the dendrites compared to the grain refined network, which could be a result of such an anisotropic coarsening process.

The coarsening exponent derived from the measurements of non equiaxed Al-Ge32 reasonably agrees with theory, yet we find a smaller exponent for the coarsening grain-refined sample. Theory predicts a $t^{1/3}$ growth of the particles, yet both 2D and 3D observations of the grain refined microstructure are closer to $t^{1/4}$~$t^{1/5}$. This was not reported by Rowenhorst et al., who extrapolated a $t^{1/3}$ coarsening kinetic from 2D plane section measurements[36] perhaps due to particulars of their system or the unavailability of true 3D data. We believe that the high solid volume fraction of the Al-Ge32 mixture in our study is the cause for a smaller exponent compared to that predicted by the LSW theory. Indeed, Rowenhorst et al hypothesize that thin liquid films might separate adjacent particles which, if relevant to our system, could lead to an increased interfacial curvature stabilizing the larger particles and reducing the growth rate.[36] Alternatively, $t^{1/4}$ and $t^{1/5}$ growth exponents have been suggested for precipitates assuming 2D and 1D diffusion mechanisms respectively.[21] And yet, it is difficult to compare such mechanisms to the findings in our system, since the inter-particle mass transport in semi-solid alloys occurs mainly by diffusion through the liquid matrix, and not via a solid phase. The measured contiguity of 0.21 shows that a significant fraction of the particles surface appears

to be connected or in close proximity to neighboring particles thereby reducing the free solid-liquid interface. Thus, it is possible that diffusion occurs through inter-particle wetting layers, which similarly to grain boundaries in solids[21], results in a reduced coarsening exponent.

Compared to the bulk samples, a slightly slower coarsening is observed for thinner foils, an effect we believe to be related to the reduced availability of the liquid phase in the microstructure. The thinner foils are characterized by a thickness that is close to the average particle size and our measurements indicate that coarsening is hindered when samples of dimensions close to the particle size distribution are annealed. Changing the solid fraction by increasing the annealing temperature for the thickest radiography sample did not have a significant effect on the coarsening rate or the exponent. As an additional measure of the statistical significance of the 2D results, we looked at the standard deviation of gray values in the radiographs taken at different annealing times. The gray levels in these images represent the attenuation of X-rays, which for a constant sample thickness, is proportional to the partition of the solid phase. Consequently the gray values distribution broadens due to the growing average particle diameter. The standard deviation of gray levels was plotted as a function of annealing time (data not shown) and fitted similarly to those in Fig 8. We obtained exponents of 0.175, 0.224, 0.233 and 0.313 for the 0.1 *mm*, 0.2 *mm*, 0.4 *mm* and 0.5 *mm* thick samples, which is remarkably close to the texture analysis results. This provides corroborating evidence to the robustness of the segmentation, labeling and image processing procedure.

We note that the particle analysis of the radiographs accurately reproduces the coarsening trend but underestimates the particle size (as can be seen by comparing the particle dimensions in 2D with the 3D results: e.g. 38 μm vs. 95 μm after 40 *min* annealing time), similar to calculating the size distribution from metallographic micrographs. Radiographic images cannot be used to determine the true particle size, only the coarsening exponent by evaluating a series of radiographic measurements. The tomography datasets on the other hand,

allow calculation of the true particle sizes as well as the coarsening kinetics (Eq. 1) including both exponent and rate. However tomography was performed on cold samples, thus the recorded series of 3D images provides only a quasi-dynamic evolution of microstructure. We point out that the remelting and cooling of the samples between two sequential tomography measurements might result in different particle growth kinetics compared to continuous coarsening. Nevertheless the good correspondence between 2D in situ and 3D cyclic annealing indicates that these differences are minor.

Our results suggest that further radiography and tomography measurements should be performed so as to provide better statistics and comparison to other alloys. These methods show great promise for furthering our knowledge about the 3D coarsening process taking place in semi-solid alloys and other phase-separating systems which are not amenable to conventional imaging methods. Ludwig et al have recently[23] shown that at very high flux x-ray sources and using a polychromatic beam, full 3D tomographic scans can be performed within minutes thus providing the necessary time-resolution for almost true dynamic coarsening experiments. Additional experiments may thus reveal the exact relation between solid volume fraction and coarsening of the solid particles.

Acknowledgements

We thank Dr. J. Goebbels, Dr. G. Weidemann, T. Wolk and M. Klinger for their important support during experiments at BESSY. Our gratitude goes to Dr. A. Haibel for administrative support. Data analysis was inspired by the work of N. Eschricht, Dr. K. Schladitz and Prof. J. Ohser. Sample preparation was done by C. Leistner and H. Kropf.

References:

1 L. Ratke and P. W. Voorhees, *Growth and Coarsening* (Springer, 2001).
2 S. Annavarapu and R. D. Doherty, Acta Metallurgica et Materialia **43,** 3207-3230 (1995).
3 W. Ostwald, Zeitschrift für Physikalische Chemie **34,** 495 (1900).
4 P. W. Voorhees, Journal of Statistical Physics **38,** 231-252 (1985).
5 P. J. Uggowitzer and H. Kaufmann, Fundamentals of Thixoforming Processes **75,** 525-530 (2004).

[6] Z. Fan, International Materials Reviews **47,** 1-37 (2002).
[7] M. C. Flemings, *Solidification Processing* (McGraw-Hill, 1974).
[8] W. K. Thieringer and L. Ratke, Acta Metallurgica **35,** 1237-1244 (1987).
[9] H. J. Diepers, C. Beckermann, and I. Steinbach, Acta Metallurgica **47,** 3663-3678 (1999).
[10] P. W. Voorhees, Annual Review of Materials Science **22,** 197-215 (1992).
[11] Y. Enomoto, K. Kawasaki, and M. Tokuyama, Acta Metallurgica **35,** 915-922 (1987).
[12] J. A. Warren and B. T. Murray, Modelling and Simulation in Materials Science and Engineering **4,** 215-229 (1996).
[13] S. Takajo, W. A. Kaysser, and G. Petzow, Acta Metallurgica **32,** 107-113 (1984).
[14] I. M. Lifshitz and V. V. Slyozov, Journal of Physical Chemistry **19,** 35-50 (1961).
[15] C. Wagner, Zeitschrift für Elektrochemie **65,** 581-591 (1961).
[16] Y. Enomoto, M. Tokuyama, and K. Kawasaki, Acta Metallurgica **34,** 2119-2128 (1986).
[17] T. L. Wolfsdorf, W. H. J. Bender, and P. W. Voorhees, Acta Materialia **45,** 2279-2295 (1997).
[18] E. Tzimas and A. Zavaliangos, Materials Science and Technology **289,** 228-240 (2000).
[19] B. Niroumand and K. Xia, Materials Science and Engineering A **283,** 70-75 (2000).
[20] E. D. Manson-Whitton, I. C. Stone, J. R. Jones, P. S. Grant, and B. Cantor, Acta Materialia **50,** 2517-2535 (2002).
[21] J. J. Hoyt, Acta metall. mater. **39,** 2091-2098 (1991).
[22] P. Fratzl, J. L. Lebowitz, O. Penrose, and J. Amar, Phys. Rev. B **44,** 4794-4811 (1991).
[23] R. Mendoza, I. Savin, K. Thornton, and P. W. Voorhees, Nature **3,** 385-388 (2004).
[24] O. Ludwig, M. DiMichiel, P. Falus, L. Salvo, and M. Suery, in *8th Int. S2P conference proceeding*, Cyprus, 2004.
[25] W. R. Loué and M. Suéry, Materials Science and Engineering A **203,** 1-13 (1995).
[26] S. K. Kailasam, M. E. Glicksman, S. S. Mani, and V. E. Fradkov, Metallurgical and Materials Transactions A **30,** 1541-1547 (1999).
[27] J. Alkemper, R. Mendoza, and P. W. Voorhees, Advanced Engineering Materials **4,** 694-697 (2002).
[28] T. B. Massalski, *Binary alloy phase diagrams*, Vol. 1 (ASM International, Ohio, 1990).
[29] S. Nafisi, R. Ghomashchi, and A. Charette, in *8th Int. S2P conference proceeding*, Cyprus, 2004.
[30] K. T. Kashyap and T. Chandrashekar, Bulletin of Materials Science **24,** 345-353 (2001).
[31] W. Görner, M. P. Hentschel, B. R. Müller, H. Riesemeier, M. Krumrey, G. Ulm, W. Diete, U. Klein, and R. Frahm, Nucl. Instr. and Meth. in Phys. Res. A **467-468,** 703-706 (2001).
[32] A. Rack, Thesis, Technical University of Berlin (2006).
[33] U. Bonse and F. Busch ,Prog. Biophys. molec. Biol. **65,** 133-169 (1996).
[34] L. Salvo, P. Cloetens, E. Maire, S. Zabler, J. J. Blandin, J. Y. Buffiere, W. Ludwig, E. Boller, D. Bellet, and C. Josserond, Nucl. Instr. Meth. in Phys Res. B **200,** 273-286 (2003).
[35] M. Stampanoni, G. Borchert, P. Wyss, R. Abela, B. Patterson, S. Hunt, S. Vermeulen, and P. Ruegsegger, Nucl. Instr. Meth. in Phys Res. A **491,** 291-301 (2002).
[36] D. J. Rowenhorst, J. P. Kuang, K. Thornton, and P. W. Voorhees, Acta Materialia **54,** 2027-2039 (2006).
[37] O. Cuisenaire and B. Macq, Computer Vision and Image Understanding **76,** 263-172 (1999).
[38] P. Soille and L. Vincent, in *SPIE Visual Communications and Image Processing*, **1360**, 240-250 (1990).
[39] L. Vincent and P. Soille, in *IEEE Transactions on Pattern analysis and Machine Intelligence* **13,** 583-598 (1991).
[40] MAVI (modular algorithms for volume images) K. Schladitz and M. Godehardt, ITWM Fraunhofer institute, Germany. http://www.itwm.fhg.de/mab/projects/MAVI/index_en.php
[41] M. D. Abramoff, P. J. Magelhaes, and S. J. Ram, Biophotonics International **11,** 36-42 (2004).
[42] P. J. Uggowitzer, G. Gullo, and A. Wahlen, (Institut für Metallforschung, Zürich, 2000), http://e-collection.ethbib.ethz.ch/ecol-pool/bericht/bericht_178.pdf
[43] R. Mendoza, K. Thornton, I. Savin, and P. W. Voorhees, Acta Materialia **54,** 743-750 (2006).

Tables and Figure captions

sample	thickness [mm]	temperature [C]	g_s	no. of images	time [min]	growth rate K	growth exponent
1	0.1	450	0.49	540	29	20.64 ± 0.25	0.1708 ± 0.0037
2	0.2	450	0.49	540	33	13.71 ± 0.18	0.2498 ± 0.0035
3	0.4	450	0.49	660	45	16.33 ± 0.11	0.2143 ± 0.0019
4	0.5	470	0.45	660	38	17.70 ± 0.14	0.2071 ± 0.0023

Table 1: Results from in situ radiography of coarsening semi-solid Al-Ge32 alloy.

sample	time [min]	no. of particles	average <d> [µm]	(SD) [µm]	ratio <d>/(SD)	cont. G^S	connectivity
Al-Ge32 + AlTiB	0	10485	70.72	14.87	4.762	0.190	4.0
Al-Ge32 + AlTiB	8	8011	77.82	16.03	4.854	0.209	3.6
Al-Ge32 + AlTiB	16	6393	83.62	17.65	4.738	0.210	3.6
Al-Ge32 + AlTiB	24	5438	88.20	18.70	4.717	0.212	3.6
Al-Ge32 + AlTiB	32	4832	91.35	20.09	4.547	0.209	3.6
Al-Ge32 + AlTiB	40	4278	94.68	20.70	4.574	0.210	3.6
Al-Ge32	0	4906	81.65	20.95	3.897	0.107	5.0
Al-Ge32	24	2977	102.15	22.53	4.534	0.160	4.0
Al-Ge32	32	2497	108.17	24.05	4.500	0.165	3.4
Al-Ge32	40	2209	112.01	25.04	4.473	0.167	3.4

Table 2: Resulting values of the particle number, average particle diameter <d>, standard deviation (SD), <d>/(SD) of the distribution function as well as maximum contiguity G^S and connectivity (determined from the fitting curves) in samples of grain refined Al-Ge32 (+ AlTiB) and non grain refined Al-Ge32 measured for different annealing times between 0 and 40 min.

Fig. 1: a) Coarsening of dispersed particles. Larger spheres grow at the expense of smaller ones. b) Coarsening of connected particles of similar size via coalescence. c) Coarsening of a network of agglomerated particles preserving its self-similar morphology.

Fig. 2: Two micrographs of polished samples showing as-cast Al-Ge32 alloy: a) microstructure with addition of 4wt.% of Al-Ti5-B grain refiner and b) without additional grain refiner.

Fig. 3: Binary phase diagram of Al-Ge alloy (the dashed line indicates the composition of Al-Ge32(wt.%) alloy). The liquidus temperature is approx. 560ºC for this composition.

Fig. 4: a) Schematic illustration of the real-time radiographic experiment at BESSY / BAM*line*. b) Image of a semi-solid Al-Ge32 foil in the BN_3 sample holder (note the horizontal stripes overlaying the image due to inhomogeneous beam intensity; the upper bright edges are due to the edge of the optical lenses).

Fig. 5: Virtual "stripe-filter" for beam normalization: Grey values representing the image intensity are represented as a z-value in a pseudo 3D topography in the (x,y)-plane. a) Every radiographic image is a superposition of underlying background and structural information. b) The background (virtual brightfield) image is characterized by horizontal stripes originating from the beam reflections by a double multilayer monochromator. c) After application of a stripe-filter we obtain an image of the structural information only.

Fig. 6: Coarsening of 0.2 *mm* thick Al-Ge32 foil in a boron nitride sample holder: a) Radiograph taken after the alloy was annealed at T=450ºC for 3 *min*, b) image of the same foil after 33 *min* annealing time in the semi-solid state, c) Metallurgical micrograph of a polished section of the same sample after annealing.

Fig. 7: a) Histogram of 8-bit grey values in a typical dataset (dashed line symbolizes the application of a threshold), b) Typical image showing Al-particles in Al-Ge matrix, c) binary image after application of median filter and threshold binarization, d) Euclidean distance transform (EDT) calculated from the binary image, e) Labeled image with watersheds calculated from the EDT, f) Multiplication of the labeled watershed image with the binary map (b) yields a labeled image of the segmented particles.

Fig. 8: The coarsening exponent from the fit of the data of the 0.5 *mm* foil as a function of different threshold values, respectively solid area fractions (confidence intervals are shown with data points).

Fig. 9: Comparison of the evolution of the mean particle diameter derived from radiographic films of four Al-Ge32 foils of increasing thicknesses: a) 0.1 *mm*, b) 0.2 *mm*, c) 0.4 *mm* and d) 0.5 *mm*. The red measurement point have been masked as they correspond to times before the coarsening started. The insets show the standard deviation of the average particle diameter as a function of annealing time.

Fig. 10: a+b) Histograms of particle diameter and Gaussian fitting curves for a) equiaxed Al-Ge32 structure and b) non equiaxed structure from the initial state up to 40 min of annealing time at 450ºC. c+d) Contiguity distributions and Gaussian fits for c) equiaxed and d) non equiaxed structure. e+f) Connectivity and log-normal fitting curves (e – equiaxed structure, f – non equiaxed).

Fig. 11: Coarsening of equiaxed microstructure of grain refined Al-Ge32: (a1-6) Small cluster of particles inside a virtual confinement of 250 μm in diameter, cut at the same position in the 6 datasets, each representing an annealing at 450ºC with a holding time of a1) 0 min (initial structure), a2) 8 min, a3) 16 min, a4) 24 min, a5) 32 min and a6) 40 min. b) Non-linear fit (dashed lines show the confidence intervals) of the average particle diameter. c) Non-linear fit for the measurements of non grain-refined Al-Ge32: d1-3) show a small cluster similar to (a1-6) for 24 min, 32 min and 40 min annealing time.

Figure 1
Click here to download high resolution image

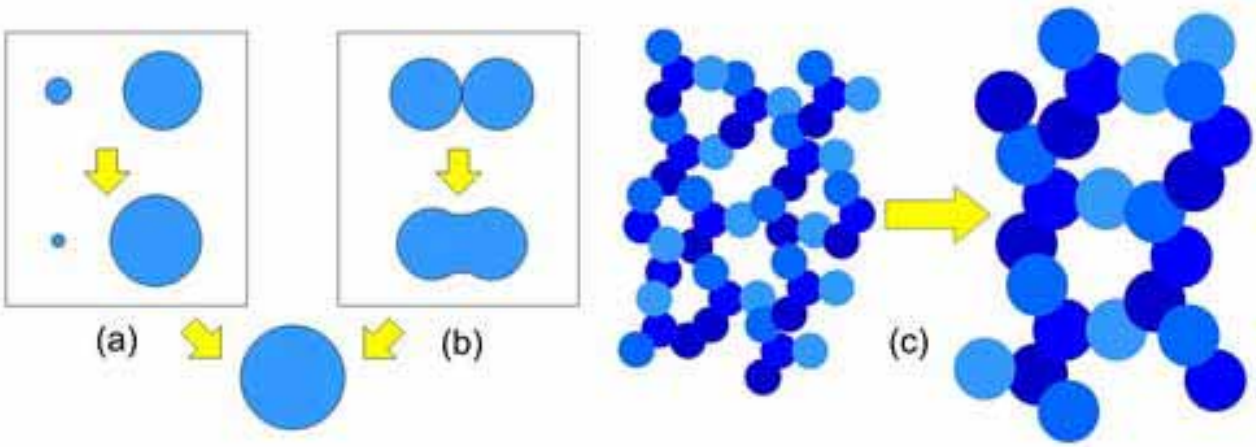

Figure 2
Click here to download high resolution image

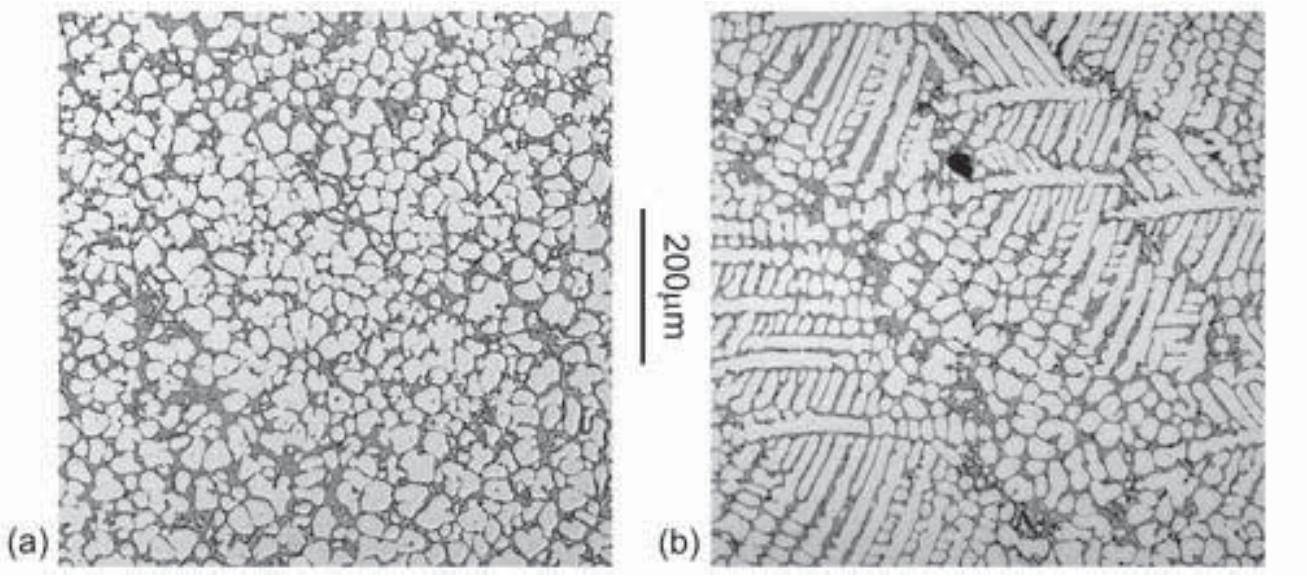

Figure 3
Click here to download high resolution image

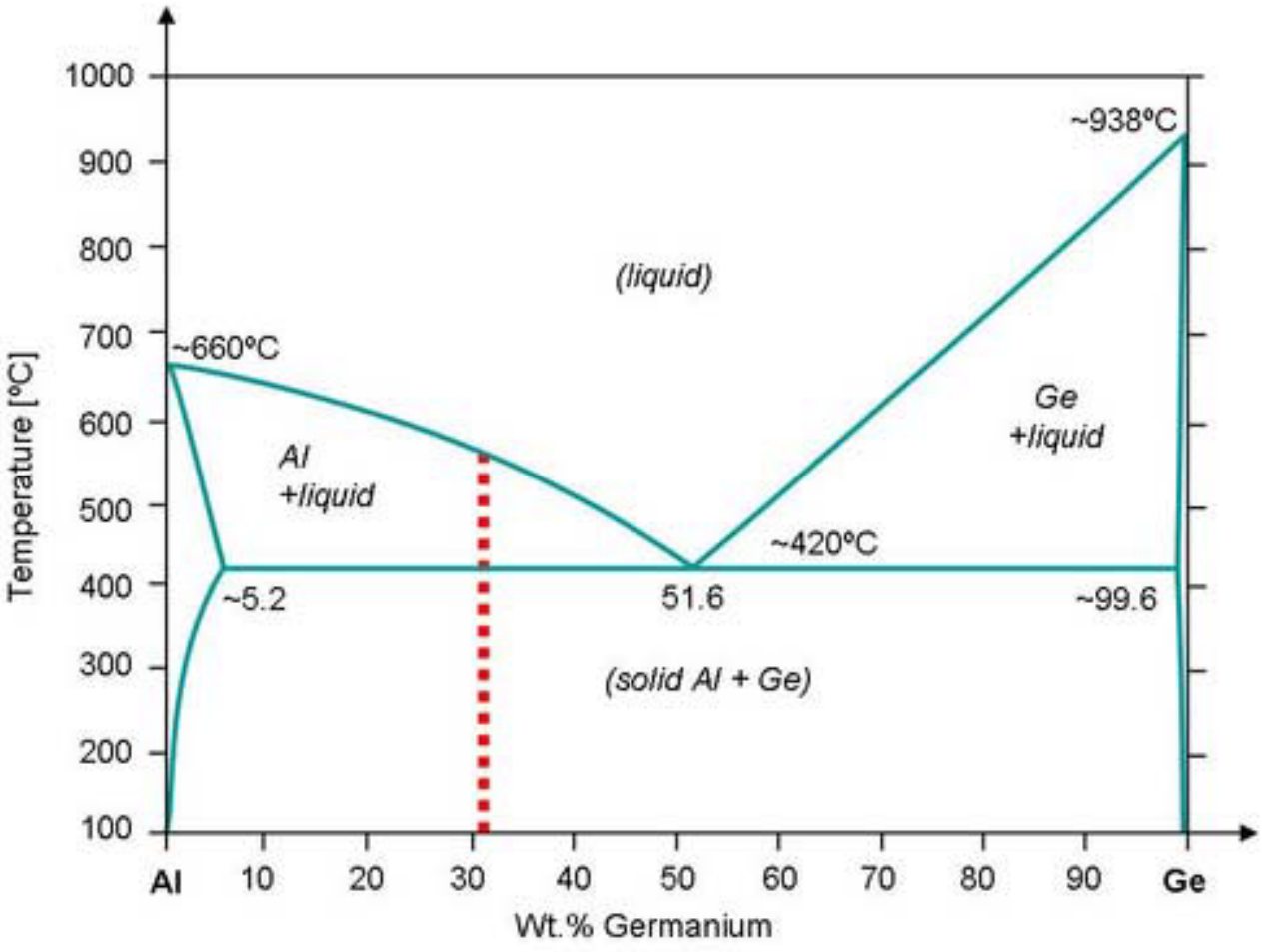

Figure 4
Click here to download high resolution image

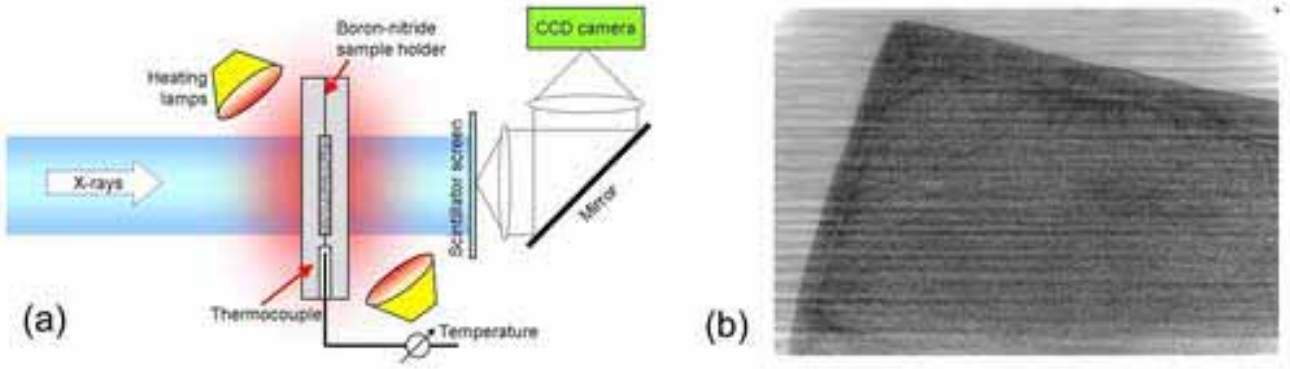

Figure 5
Click here to download high resolution image

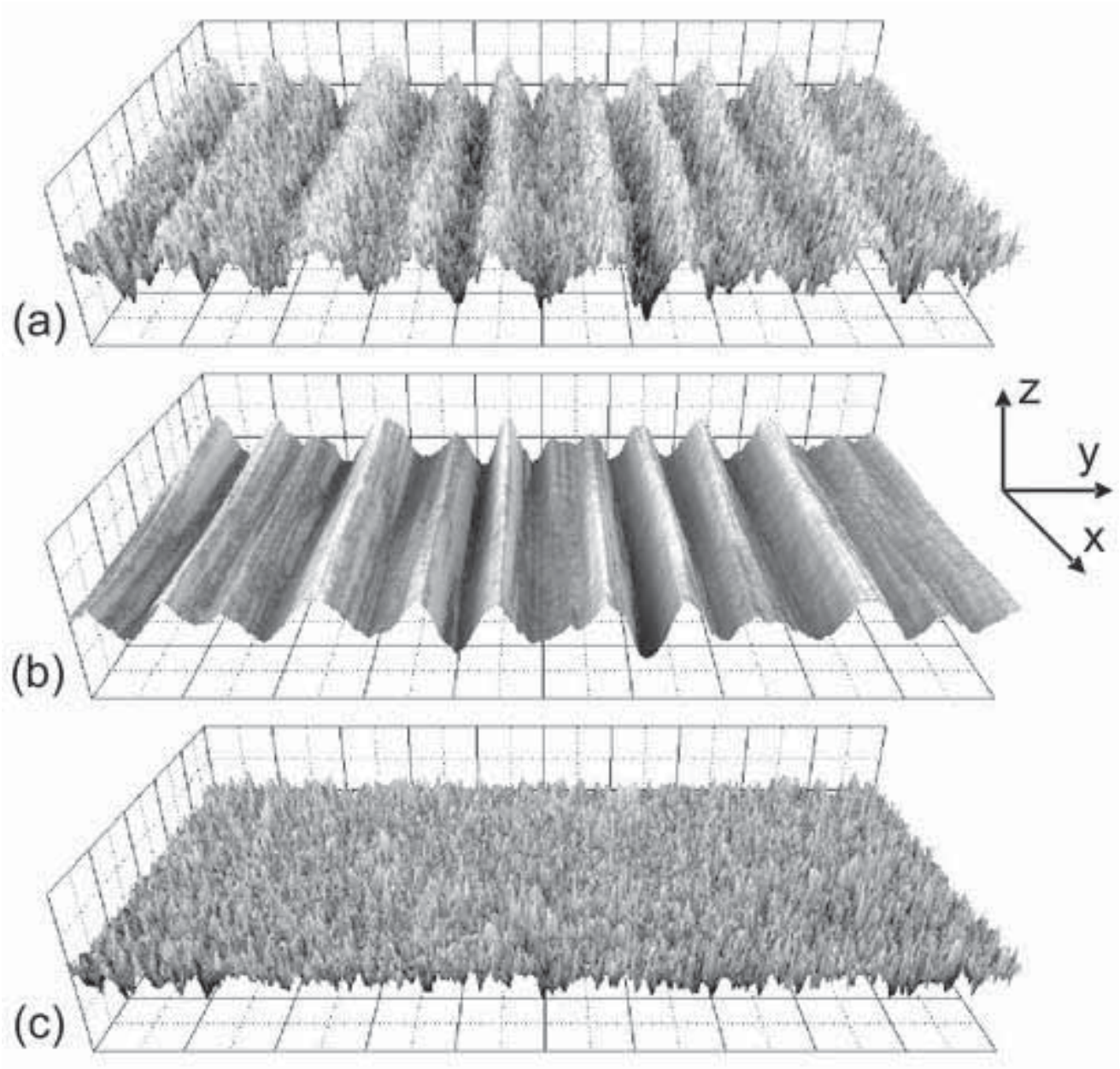

Figure 6
Click here to download high resolution image

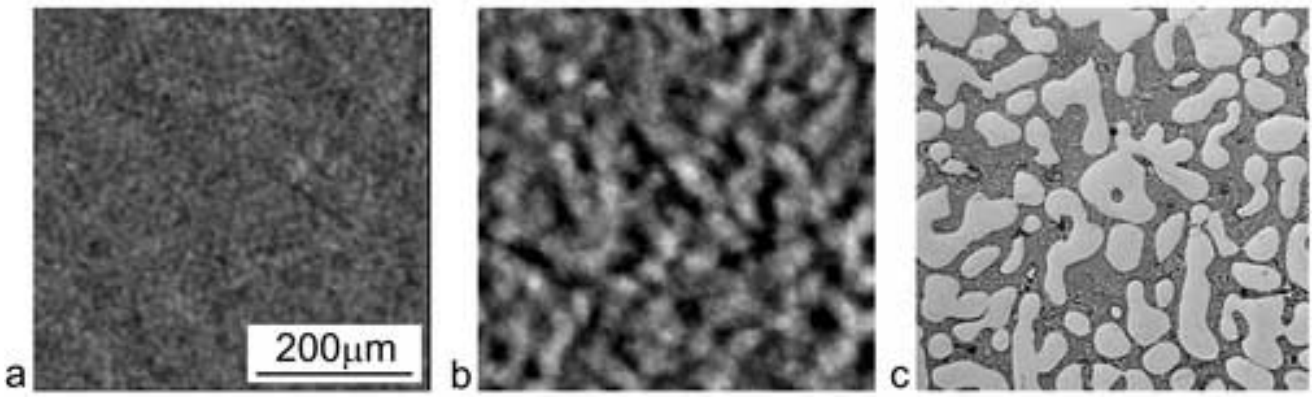

Figure 7

Click here to download high resolution image

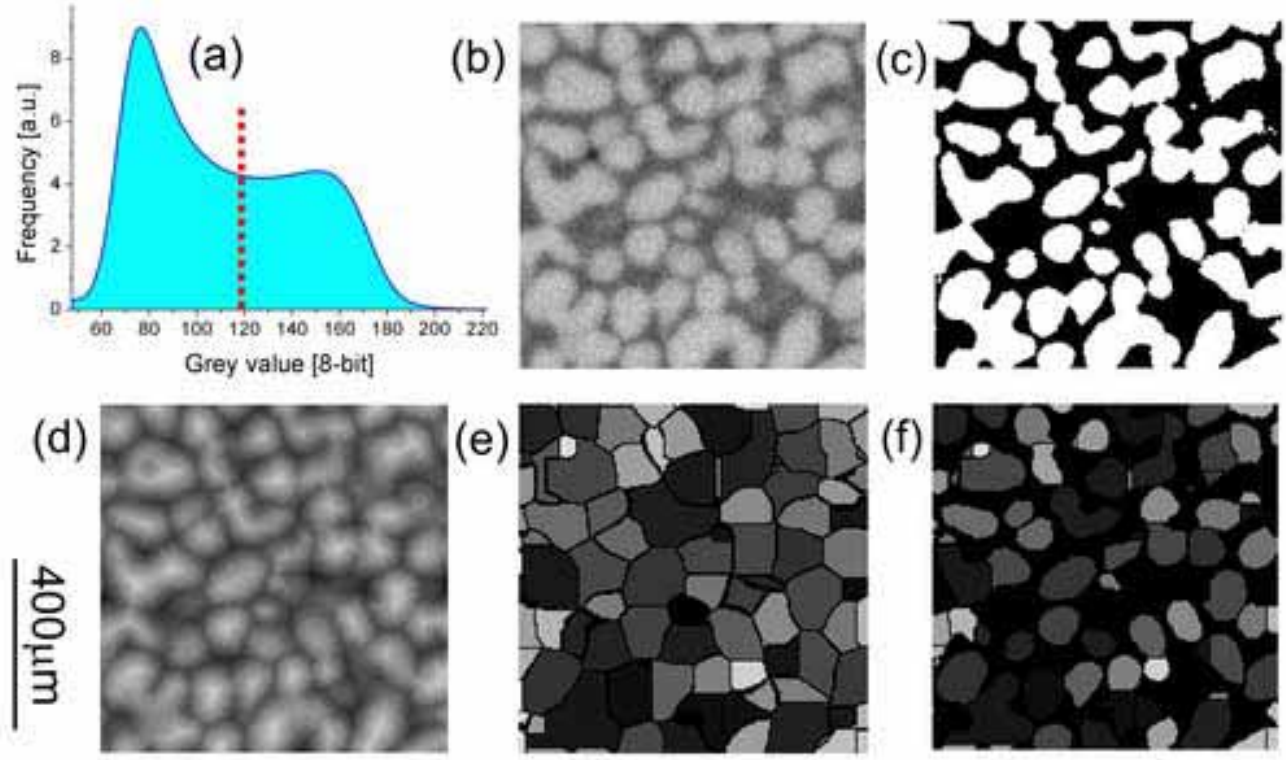

Figure 8

Click here to download high resolution image

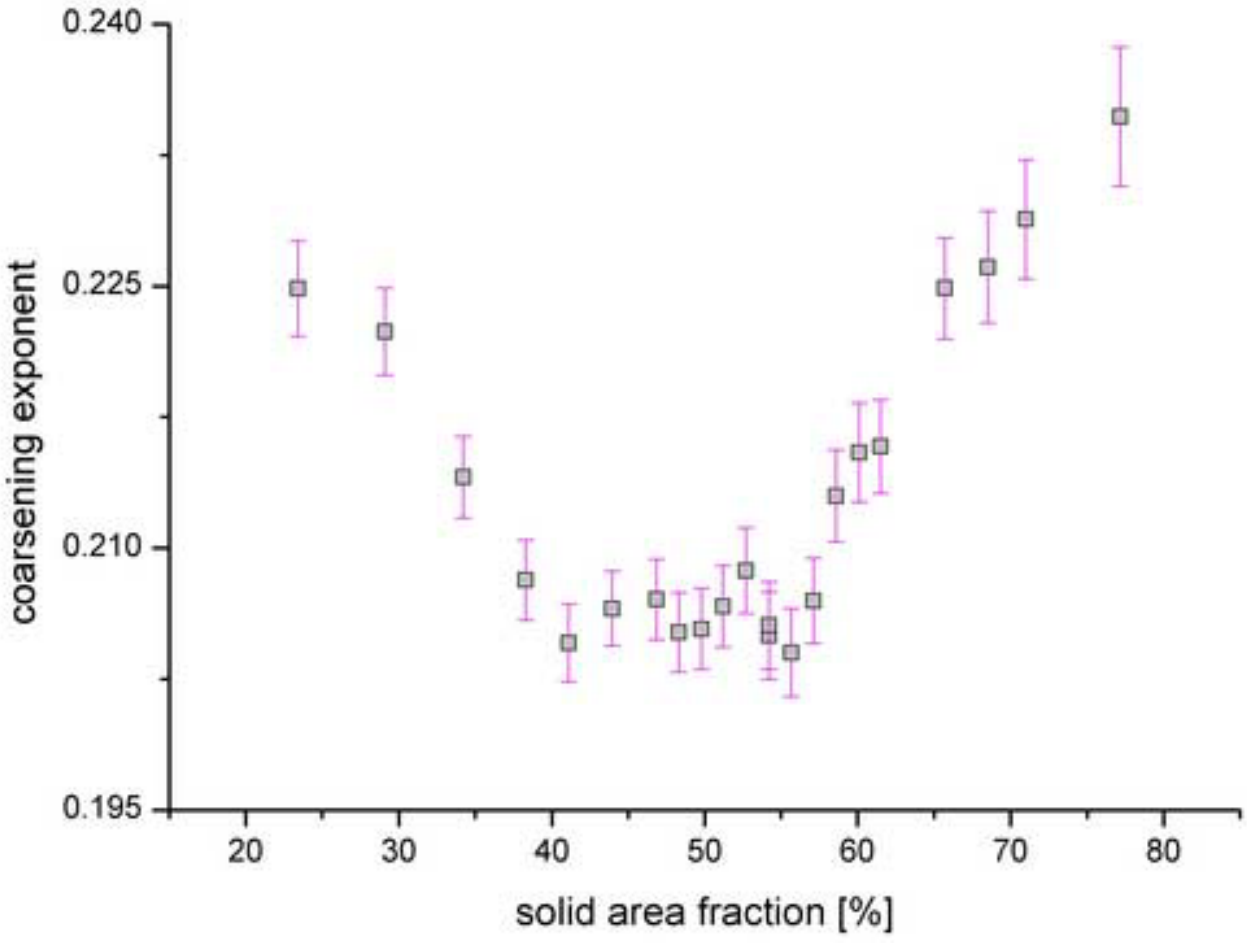

Figure 9

Click here to download high resolution image

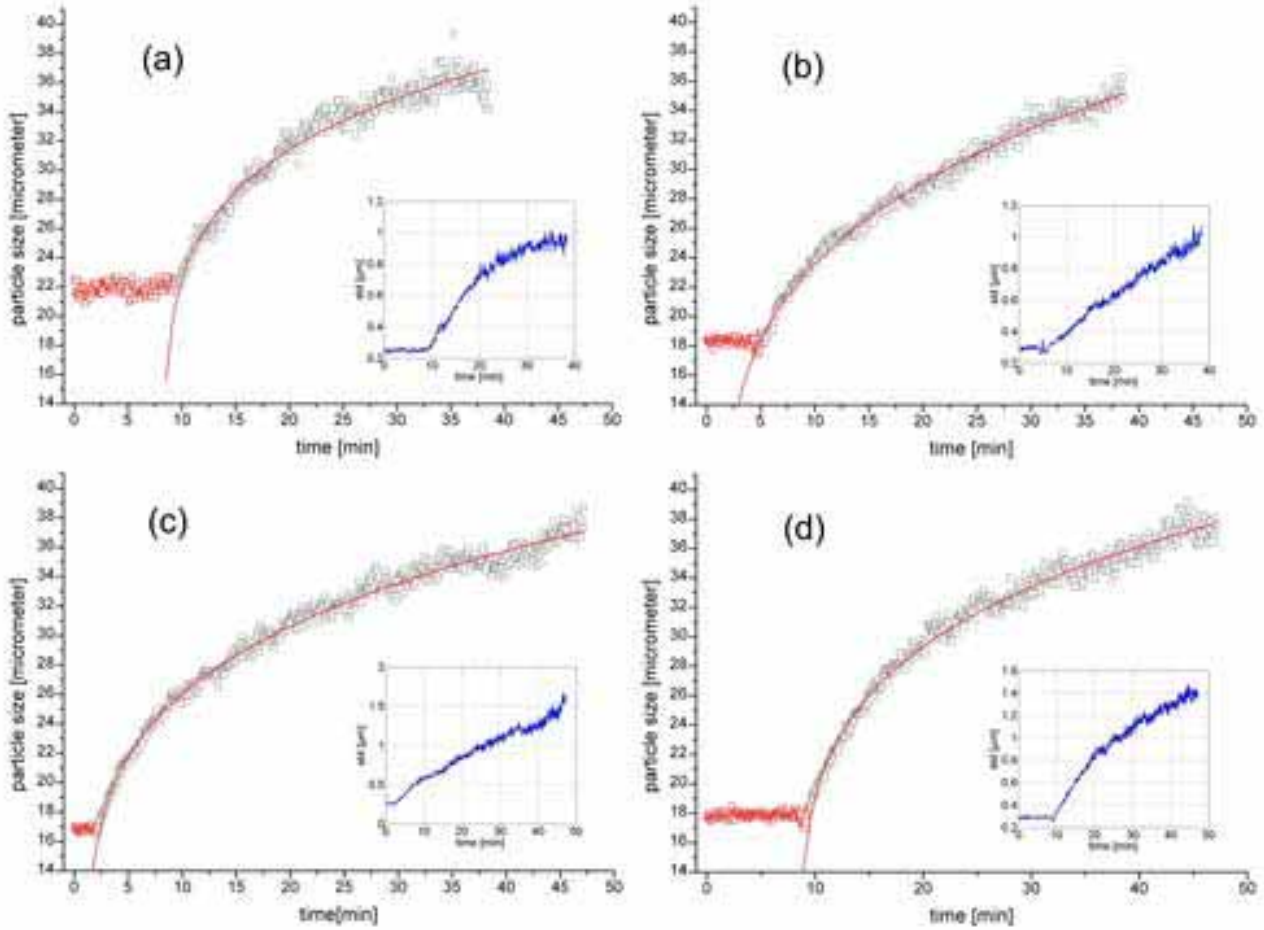

Figure 10

Click here to download high resolution image

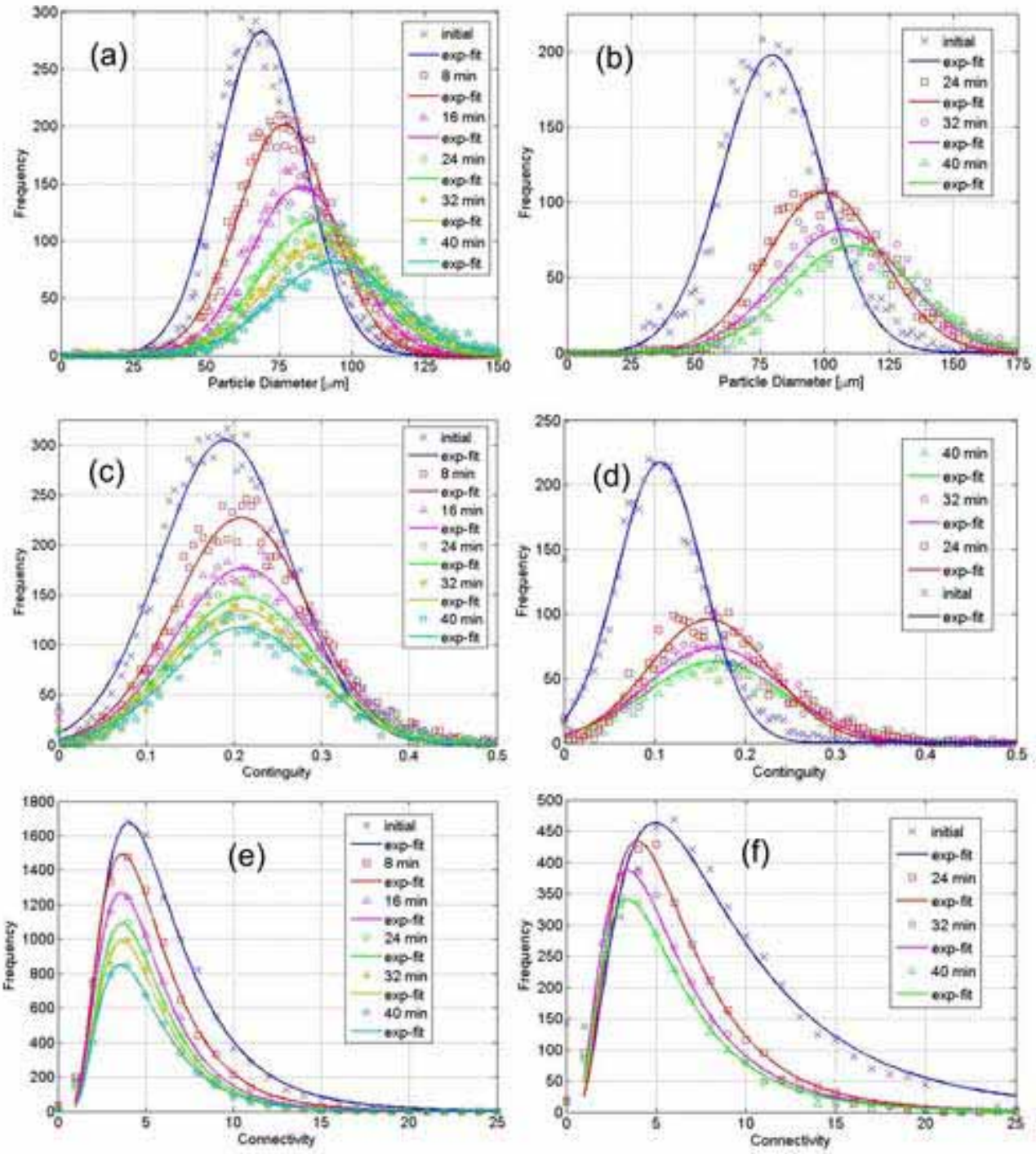

Figure 11

Click here to download high resolution image